N.F

NASA Technical Memorandum 81613

Supersonic Stall Flutter of High Speed Fans

J. J. Adamczyk and W. Stevans
Lewis Research Center
Cleveland, Ohio

and

R. Jutras
General Electric Company
Evendale, Ohio

Prepared for the
Twenty-sixth Annual International Gas Turbine Conference
sponsored by the American Society of Mechanical Engineers
Houston, Texas, March 8-12, 1981

NASA

SUPERSONIC STALL FLUTTER OF HIGH SPEED FANS

J. J. Adamczyk and W. Stevans

National Aeronautics and Space Administration
Lewis Research Center
Cleveland, Ohio

and

R. Jutras

General Electric Company
Evendale, Ohio

INTRODUCTION

Flutter can result in costly (both in time and money) overruns in turbofan-engine development programs. Solving the problem of flutter (at the engine development stage) may well mean major engine redesign and retesting. For this reason, engine manufacturers and government agencies are currently supporting numerous research programs in an attempt to develop flutter prediction systems that can be used to design flutter-free engines. To date, these research programs have identified five regions of the compressor performance map where flutter is generally encountered (fig. 1).

Of the five regions shown in figure 1, the supersonic low back-pressure flutter region has been the most thoroughly investigated analytically (refs. 1 to 3). In general, these analyses have considered the flow field through a cascade of two-dimensional airfoils undergoing simple harmonic pitching or plunging. The gas stream was assumed to be an inviscid, nonconducting, perfect gas. Shock waves that originated in the flow field were assumed to be weak so that supersonic small-disturbance theory could be used. Although these assumptions appear to oversimplify the flow conditions encountered by a rotor at the onset of flutter, the flutter boundaries predicted by these analyses correlate well with experimental data.

A recent analysis (ref. 4) has attempted to apply the supersonic, linearized, small-disturbance theory to higher backpressure operating conditions (i.e., region IV of fig. 1) by including a finite-strength shock wave within the cascade passage. Results from this analysis show that the unsteady motion of the shock wave tends to induce bending flutter. The existence of this flutter mode is documented in reference 5.

The remaining operating region where supersonic flutter occurs (region V of fig. 1) lies close to the stall line of a stage. Analyses of this region have not appeared in the open literature. Literature on this subject (e.g., refs. 5 to 7) generally presents experimental data to document the extent of the flutter region. These data provide a very limited base from which an empirical correlation can be derived for predicting the onset of this flutter mode.

The objective of the present analysis is to develop a model for predicting the onset of supersonic stall flutter encountered by rotors that do not have part-span dampers or tip shrouds. Experimental data reveal that the flutter mode is generally the first flexural mode at a reduced frequency (based on tip relative velocity and tip semichord) of about 0.2. The vibratory pattern around the rotor tends to be very regular: All blades vibrate at the same frequency but are shifted in phase by a positive interblade phase angle of about 20° to 50° (ref. 7). This positive phase shift implies that the vibratory pattern is traveling around the wheel in the direction of rotation (i.e., a forward-traveling wave).

A further characteristic of the flow regime associated with stall flutter is shown by the steady-state pressure distribution in figure 2. This pressure distribution was produced from measurements taken across a rotor tip while the rotor was operating near the flutter boundary. This figure clearly indicates a detached, leading-edge bow shock wave impinging on the suction surface of the adjacent blade. The large extent of the compression region at the base of the shock wave seems to suggest a separated flow region that would increase in size as the fan operating point moved toward the supersonic stall bending flutter boundary.

The present analysis develops a flutter model for the highly complicated flow field illustrated in figure 2 by using two-dimensional actuator disk theory. The effects of flow separation are included in the model through rotor-loss and deviation-angle correlations. For low-speed flows, actuator disk flutter models have been able to predict the onset of a single-degree-of-freedom bending flutter mode (e.g., refs. 8 and 9). The success of the models at low speeds suggests that a compressible actuator disk model might be capable of predicting the onset of bending flutter at supersonic speeds. This hypothesis has been confirmed by a number of calculations. These calculations, however, did require as input the interblade phase angle at the onset of flutter. So that this requirement could be avoided, the actuator disk model was modified to allow for moderate values of interblade phase angle. This modification results in a flutter model that can be developed into a flutter prediction system. The validity of this flutter prediction system is demonstrated by comparing the predicted flutter boundary of a high-speed fan stage with its measured boundary.

FORMULATION

The present analysis for stall bending flutter of an isolated rotor models the rotor as a two-dimensional cascade of airfoils. The cascade is defined by the blade-element geometry on a cylindrical surface at a distance R from the axis of rotation. The flow field in the cascade plane is assumed to be two dimensional, compressible, and time dependent. Viscous forces are considered only within the blade channel. The unsteady flow variables associated with the rotor vibratory motion are assumed to be smaller than their steady-state counterparts. These variables at an instant in time are required to be periodic around the wheel at a period equal to a fractional part of the circumferential distance $d = 2\pi R$.

The motion of the airfoils in the cascade plane is restricted to simple harmonic plunging and edgewise motion at a cyclic frequency ω (fig. 3). In addition the motion of each airfoil at an instant in time is assumed to be shifted from that of its neighbor by an interblade phase angle of $\sigma = 2\pi n/N$, where n is an integer and N is the number of blades in the rotor. In the present analysis the reduced-frequency parameter k_b and the interblade phase angle are assumed to be small. (Reduced frequency $k_b = \omega b/\bar{q}_{-\infty}$, where b is the semichord of an airfoil and $\bar{q}_{-\infty}$ is the magnitude of the relative inlet velocity in the cascade plane.)

Field Equations

The governing linearized equations for the flow field upstream and downstream of the cascade are written with respect to the relative coordinate system. The variables in these equations are nondimensionalized by the steady inlet speed $\bar{q}_{-\infty}$, the circumferential distance around the wheel d, the inlet steady-state fluid density $\bar{\rho}_{-\infty}$, and the inlet steady-state fluid temperature $\bar{T}_{-\infty}$. In addition the subscripts $(\infty, -\infty)$ signify downstream and upstream flow variables.

The linearized continuity equation for the upstream and downstream flow fields is

$$\frac{\partial \tilde{\rho}_{\pm\infty}}{\partial t} + \bar{U}_{i,\pm\infty}\frac{\partial \tilde{\rho}_{\pm\infty}}{\partial X_i} + \bar{\rho}_{\pm\infty}\frac{\partial \tilde{U}_{i,\pm\infty}}{\partial X_i} = 0 \qquad (1)$$

where the tilde denotes a time-dependent variable and the bar signifies a steady-state variable. The variables ρ, U_i, t, and X_i are the density, velocity components, time, and spacial coordinates, respectively. (See fig. 3 for definition of coordinate system.) In addition the use of repeated indices denotes summation with respect to the repeated index. The linearized momentum equations for the flow fields are

$$\frac{\partial \tilde{U}_{i,\pm\infty}}{\partial t} + \bar{U}_{j,\pm\infty}\frac{\partial \tilde{U}_{i,\pm\infty}}{\partial X_j} = -\frac{1}{\bar{\rho}_{\pm\infty}}\frac{\partial \tilde{P}_{\pm\infty}}{\partial X_i} \qquad i = 1, 2 \qquad (2)$$

where $\tilde{P}_{\pm\infty}$ is the nondimensional pressure. The remaining field equations are the energy equation for an inviscid, nonconducting gas

$$\frac{\partial \tilde{s}_{\pm\infty}}{\partial t} + \bar{U}_{i,\pm\infty}\frac{\partial \tilde{s}_{\pm\infty}}{\partial X_i} = 0 \qquad (3)$$

and the equation of state

$$\bar{s}_{\pm\infty} = \frac{1}{\bar{M}^2_{-\infty}\gamma}\frac{1}{\gamma - 1}\frac{\tilde{P}_{\pm\infty}}{\bar{P}_{\pm\infty}} + \frac{1}{\gamma - 1}\frac{1}{\bar{M}^2_{-\infty}}\frac{\tilde{\rho}_{\pm\infty}}{\bar{\rho}_{\pm\infty}} \qquad (4)$$

The variables appearing in equations (3) and (4) are the entropy s; the ratio of specific heats γ; and the inlet steady-state relative Mach number $\bar{M}_{-\infty}$. (The entropy was nondimensionalized with respect to $\bar{T}_{-\infty}/\bar{q}^2_{-\infty}$.)

The present analysis assumes that there are no sources of entropy or vorticity upstream of the cascade. The upstream, unsteady velocity field must therefore be irrotational and hence is equal to the gradient of a potential function $\tilde{\phi}_{-\infty}$ where

$$\tilde{U}_{i,-\infty} = \frac{\partial \tilde{\phi}_{-\infty}}{\partial X_i} \qquad i = 1, 2 \qquad (5)$$

The unsteady velocity field downstream of the cascade is expressed as

$$\tilde{U}_{i,\infty} = \frac{\partial \tilde{\phi}_{\infty}}{\partial X_i} + \tilde{U}^R_{i,\infty} \qquad i = 1, 2 \qquad (6)$$

where $\partial\tilde{\phi}_{\infty}/\partial X_i$ represents the irrotational component of the field and $\tilde{U}^R_{i,\infty}$ its rotational component. The source of the rotation field is the vorticity shed by the oscillating airfoils.

The solution to the field equations is obtained by assuming a simple harmonic spacial and temporial dependency for the potential, the rotational velocity fields and the dowrstream entropy field. The details of the solution procedure can be found in reference 10.

Boundary Conditions

It is shown in reference 10 that four boundary conditions must be specified at the actuator disk to relate the unsteady flow field to the cascade deformation and the steady inlet flow conditions.

The first of these boundary condition requires the flow to be continuous across the deforming disk. The analytical form of this boundary condition is

$$(1 + \tilde{\rho}_{-\infty})U^{Rel}_{n,-\infty} = (\bar{\rho}_{\infty} + \tilde{\rho}_{\infty})U^{Rel}_{n,\infty} \qquad \text{at } X_1 = 0 \qquad (7)$$

where $U^{Rel}_{n,\infty}$ represents the normal velocity components relative to the deforming disk. These velocity components to first order (i.e., small cascade-plane deflection) are equal to

$$U^{Rel}_{n,-\infty} = \bar{U}_{1,-\infty} + \frac{\partial\tilde{\phi}_{-\infty}}{\partial X_1} - \frac{\partial\tilde{h}_1}{\partial t} - \bar{U}_{2,-\infty}\frac{\partial\tilde{h}_1}{\partial X_2} \qquad (8)$$

$$U^{Rel}_{n,\infty} = \bar{U}_{1,\infty} + \frac{\partial\tilde{\phi}_{\infty}}{\partial X_1} - \frac{\partial\tilde{h}_1}{\partial t} - \bar{U}_{2,\infty}\frac{\partial\tilde{h}_1}{\partial X_2} + \tilde{U}^{R}_{1,\infty} \qquad (9)$$

where $\tilde{h}_1$ is the displacement of the disk from its mean position in the axial (X_1) direction (fig. 4).

The next boundary condition requires the total enthalpy with respect to the deforming actuator disk to be locally conserved across the disk. The equivalent mathematical statement is

$$\frac{1}{\gamma - 1}\frac{1}{M^2_{-\infty}}T_{-\infty} + \frac{1}{2}q^{2,Rel}_{-\infty}$$

$$= \frac{1}{\gamma - 1}\frac{1}{M^2_{-\infty}}T_{\infty} + \frac{1}{2}q^{2,Rel}_{\infty} \qquad \text{at } X_1 = 0 \qquad (10)$$

where $T_{\pm\infty}$ is the upstream and downstream gas temperature and $q^{Rel}_{\pm\infty}$ is the magnitude of the relative velocity approaching and leaving the disk. The expressions for $q^{Rel}_{\pm\infty}$ are

$$q^{Rel}_{-\infty} = \left[\left(\bar{U}_{1,-\infty} + \frac{\partial\tilde{\phi}_{-\infty}}{\partial X_1} - \frac{\partial\tilde{h}_1}{\partial t}\right)^2 + \left(\bar{U}_{2,\infty} + \frac{\partial\tilde{\phi}_{-\infty}}{\partial X_2} - \frac{\partial\tilde{h}_2}{\partial t}\right)^2\right]^{1/2} \qquad (11)$$

$$q^{Rel}_{\infty} = \left[\left(\bar{U}_{1,\infty} + \frac{\partial\tilde{\phi}_{\infty}}{\partial X_1} + \tilde{U}^{R}_{1,\infty} - \frac{\partial\tilde{h}_1}{\partial t}\right)^2 + \left(\bar{U}_{2,\infty} + \frac{\partial\tilde{\phi}_{\infty}}{\partial X_2} + \tilde{U}^{R}_{2,\infty} - \frac{\partial\tilde{h}_2}{\partial t}\right)^2\right]^{1/2} \qquad (12)$$

where $\tilde{h}_2$ is the local displacement of the cascade in the tangential (X_2) direction (fig. 4).

The third boundary condition requires that the local inlet and exit flow angles relative to the deforming disk satisfy a deviation angle correlation of the form

$$\delta = g(\alpha, M_{-\infty}, \mu, \theta') \qquad (13)$$

where α is the local, relative incidence angle, $M_{-\infty}$ is the local, relative inlet Mach number, μ is the local solidity of the deformed cascade, and θ' is the local stagger angle measured from the normal to the leading-edge plane (fig. 4). The local, relative incidence angle is related to the local, relative inlet flow angle $\beta_{-\infty}$ measured from the normal to the leading-edge plane by the equation

$$\alpha = \beta'_{-\infty} - \theta' - \delta_{m_1} \qquad (14)$$

The variable δ_{m_1} in this equation is the angle between the chord line and the tangent to the camber line at the leading edge. The corresponding relation for the local deviation angle is

$$\delta = \beta'_{\infty} - \theta' - \delta_{m_2} \qquad (15)$$

where β'_{∞} is the local, relative exit flow angle measured from the normal to the trailing-edge plane and δ_{m_2} is the angle between the chord line and the tangent to the camber line at the trailing edge.

Relationships for the angles, inlet Mach number and cascade solidity in the above equations are derived by expanding these variables along with equations (13), (14) and (15) to first order. The details of this expansion can be found in reference 10.

The last boundary condition specifies the local entropy that is generated as the fluid passes through the cascade. The loss associated with the local entropy rise is defined in terms of a loss coefficient defined as

$$\chi = \frac{P^{Rel}_{0,-\infty} - P^{Rel}_{0,\infty}}{\frac{1}{2}\rho_{-\infty}q^{2,Rel}_{-\infty}} \qquad (16)$$

The variable $P^{Rel}_{0,-\infty} - P^{Rel}_{0,\infty}$ in this equation represents the local total-pressure loss measured relative to the deforming actuator disk. The entropy rise across the disk is related to this quantity by the equation of state

$$P^{Rel}_{0,-\infty} - P^{Rel}_{0,\infty} = P^{Rel}_{0,-\infty}\left(1 - e^{-\gamma M^2_{-\infty}s_{\infty}}\right)$$

Thus s_{∞} must be equal to

$$s_{\infty} = -\frac{1}{\gamma M^2_{-\infty}}\ln\left(1 - \frac{1}{2}\frac{\rho_{-\infty}q^{2,Rel}_{-\infty}}{P_{0,-\infty}}\chi\right) \qquad (17)$$

The analysis assumes that the local loss coefficient χ is related to the local inlet flow field, as observed with respect to the deforming disk, by a relationship of the form

$$\chi = \chi(\alpha, M_{-\infty}, \mu, \theta') \qquad (18)$$

As in equation (13) the parameters appearing in this equation can be related to the unsteady flow field approaching the cascade and the cascade deformation. Upon combining equation (17) with equation (18) the entropy rise across the cascade can be evaluated in terms of these perturbed quantities.

Aerodynamic Force

Having described the procedure for determining the flow field surrounding the cascade, the unsteady forces acting on the cascade and hence its stability can be assessed. The aerodynamic force acting on the cascade is obtained by considering the flow field through a control volume that is fixed to a cascade passage (fig. 3). The present analysis assumes that the relative motion between neighboring airfoils, a measure of which is the interblade phase

angle, is small and that the reduced frequency of this motion is also small. The first assumption implies that the spatial variations of the flow variables across a cascade passage are small and thus can be neglected. The low-frequency assumption suggests that the rate of change of mass and momentum within the control volume is smaller than the net mass and momentum flux across the control volume surface and thus will also be neglected. Based on these considerations the linearized momentum equation for the control volume illustrated in figure 3 can be written as

$$\tilde{F}_1 = (\tilde{p}_{-} - \tilde{p}_{-\infty})\bar{\tau} + (\bar{p}_{-} - \bar{p}_{-\infty})\tilde{\tau}$$

$$+ \bar{W}^{Rel}(\tilde{U}_{1,-} - \tilde{U}_{1,-\infty}) + \tilde{W}(\bar{U}_{1,-} - \bar{U}_{1,-\infty}) \qquad (19)$$

$$\tilde{F}_2 = (\tilde{p}_{-} - \tilde{p}_{-\infty})\bar{\tau}\tilde{n}_2$$

$$+ \bar{W}^{Rel}(\tilde{U}_{2,-} - \tilde{U}_{2,-\infty}) + \tilde{W}(\bar{U}_{2,-} - \tilde{U}_{2,-\infty}) \qquad (20)$$

where $\tilde{F}_1$ is the force exerted by the airfoils on the control volume, τ is the pitch of the cascade, W^{Rel} is the mass flow exiting the control volume, and n_1 is the unit vector normal to the exit plane of the control volume. (This equation can be derived by expanding the quasi-steady momentum equations for the control volume shown in figure 3 to first order in perturbed variables. The details can be found in reference 10.)

The work done by the aerodynamic force on an airfoil over a cycle of motion is equal to

$$W_{Aero} = -\frac{1}{2} Re\left[\int_0^{2\pi/k} \left(\tilde{F}_1 \frac{\partial \tilde{h}_1^*}{\partial t} + \tilde{F}_2 \frac{\partial \tilde{h}_2^*}{\partial t}\right) dt\right] \qquad (21)$$

where $Re\,[\ ]$ denotes the real part of the expression and the asterisk superscript signifies the complex conjugate of the variable. The airfoil's motion can be described by

$$\tilde{h}_1 = h_1 e^{ik_2 X_2} e^{ikt}$$

$$\tilde{h}_2 = h_2 e^{ik_2 X_2} e^{ikt}$$

where k_2, the wave number in the X_2 direction, is equal to $k_2 = 2\pi n$. Equation (21) can be integrated to yield

$$W_{Aero} = -Im\left(\tilde{F}_1 \tilde{h}_1^*\right) \qquad (22)$$

where $Im\,[\ ]$ represents the imaginary part of the expression within the brackets. At the onset of flutter the aerodynamic work per cycle is equal to the mechanical energy dissipated over a cycle. If the mechanical dissipative force is proportional to the velocity of the airfoil, the mechanical energy dissipated over a cycle of motion is

$$W_D = \frac{C}{2\bar{\rho}_{-\infty}\bar{q}_{-\infty}d} Re\left[\int_0^{2\pi/k} \left(\frac{\partial \tilde{h}_1}{\partial t}\frac{\partial \tilde{h}_1^*}{\partial t} + \frac{\partial \tilde{h}_2}{\partial t}\frac{\partial \tilde{h}_2^*}{\partial t}\right) dt\right] \qquad (23)$$

where the damping coefficient C is defined as

$$C = \frac{\delta M_b}{2\pi} k \frac{\bar{q}_{-\infty}}{d} \qquad (24)$$

The variable δ in this equation is the log decrement of the mechanical damping, and M_b is the mass per unit length of a rotor blade. This variable is defined as

$$M_b = K\rho_b \tau c \qquad (25)$$

where K is a constant of proportionality, ρ_b is the blade density, τ is the average thickness of the blade, and c is its average chord length. Introducing this equation along with equation (24) into the integrated form of equation (23) yields

$$W_D = 2\delta K\left(\frac{\rho_b}{\bar{\rho}_{-\infty}}\right)\frac{\tau}{c} k_b^2 \left(\tilde{h}_1\tilde{h}_1^* + \tilde{h}_2\tilde{h}_2^*\right) \qquad (26)$$

Equating equation (26) with equation (22) and solving for δ establishes the minimum level of mechanical damping required for stability at an operating point as

$$\delta_{Onset} = -\frac{\pi}{2K}\left(\frac{\bar{\rho}_{-\infty}}{\rho_b}\right)\frac{1}{\frac{\tau}{c}} \frac{1}{k_b^2\left(h_1 h_1^* + h_2 h_2^*\right)} Min_{k_2}\left[Im\left(\tilde{F}_2\tilde{h}_2^*\right)\right] \qquad (27)$$

The symbol Min_{k_2} denotes the minimum value of the function with respect to k_2. If the available mechanical damping of a rotor blade exceeds this critical level, any small bending motion imparted to the blade will decay in time. Hence the system is stable and flutter will not occur. However, if δ_{Onset} is greater than the available mechanical damping of a rotor blade, any small bending motion imparted to the blade will cause the blade to flutter.

RESULTS

For the flutter mode under study the amplitude of the motion increases monotonically along the blade span from the node line. For blades that are rigidly fixed at their root (i.e., mechanically constrained), the node line can be assumed to lie outboard of the blade platform (i.e., outboard of the aerodynamic hub of the blade). The node line of the first flexural mode of the rotor to be investigated later in this section is approximately 20 percent of span height outboard of the platform. Thus, the vibratory motion of the blade in the rotor at any spanwise section is

$$h_1 = -\zeta \sin \bar{\theta}'(20\%) \qquad (28)$$

$$h_2 = \zeta \cos \bar{\theta}'(20\%) \qquad (29)$$

where ξ is the amplitude of the motion at the section and $\bar{\theta}'(20\%)$ is the stagger angle at 20 percent of span.

The aerodynamic work per unit of span at a given radial location depends on the amplitude of the motion of the section and the relative dynamic pressure of the incoming streamline to the section. Thus because both increase with distance from the hub, the total work done by the airstream on a blade is strongly influenced by the unsteady flow field surrounding the tip region. A simple calculation shows that this influence is concentrated in the outer 25 percent of the span. If the outer-casing boundary layer is assumed to influence the flow field over 5 percent of the tip region of a blade, a direct correlation might exist between the flutter boundary of a rotor and a two-dimensional cascade whose geometry and dynamic response coincide with that of the rotor at 85 percent of span (i.e., algebraic mean of 75 and 95 percent of span). The results presented in the remainder of this section are based on this premise.

The objective of the first series of calculations is to establish the influence of reduced frequency k_b and interblade phase angle on the aeroelastic stability of a cascade of airfoils. For this study a normalized damping parameter defined as

$$\delta_N = -\frac{1}{2}\frac{\bar{\rho}_{-\infty}}{\bar{\rho}_{0,Amb}}\frac{1}{k_b^2}\frac{v}{\xi}\left[-\sin\bar{\theta}'(20\%)\,\mathrm{Im}\left(\bar{F}_1\, e^{-ik_2X_2}\, e^{-ikt}\right)\right.$$

$$\left. + \cos\bar{\theta}'(20\%)\,\mathrm{Im}\left(\bar{F}_2\, e^{-ik_2X_2}\, e^{-ikt}\right)\right] \qquad (30)$$

is calculated as a function of k_b and the interblade phase angle. The parameter $\bar{\rho}_{0,Amb}$ in this equation is the inlet stagnation density measured in the absolute coordinate system. For δ_N greater than zero the airstream is supplying energy to the cascade. If the mechanical damping of the cascade system is zero, the operating condition would be unstable. For values of δ_N less than zero the cascade is doing work on the airstream, and hence the system is stable.

Solving equation (30) requires as input information the steady-state inlet flow properties, the geometry of the cascade, and the frequency of oscillation. A set of loss and deviation-angle correlations must also be specified. The present analysis makes use of the correlations derived in reference 10. The steady-state inlet flow conditions are derived from the blade-element data, measured at 85 percent of design speed, of the second stage of the NASA 1450-ft/sec-tip-speed two-stage fan. This blade-element data set is reported in reference 5. The cascade geometry represents the geometry of the second-stage rotor element at 85 percent of span height from the hub.

Figure 5 shows a plot of δ_N as a function of interblade phase angle and reduced frequency k_b for the second stage rotor operating at the flutter-boundary at 85 percent of design speed. This figure shows that the bending flutter mode is associated with a positive interblade phase angle (i.e., implies that the vibration pattern is traveling around the rotor in the direction of rotation). The figure also shows that increasing the reduced frequency stabilizes the motion at a constant interblade phase angle.

Figure 6 shows a plot of δ_N as a function of interblade phase angle and percentage of design weight flow along the 85-percent-speed line. For a given interblade phase angle, decreasing the weight flow at constant wheel speed (i.e., increasing the steady-state aerodynamic loading) tends to destabilize the rotor.

The results presented in figures 5 and 6 are also consistent with the observed characteristics of supersonic bending flutter reported in reference 7.

A deficiency of the present theory, as shown by the results in figures 5 and 6, is that it predicts the damping, δ_N to increase monotonically with interblade phase angle. This trend is physically unrealistic, and is a consequence of the small interblade phase angle assumption inherent in actuator disk theory. To overcome this deficiency an additional assumption was incorporated into the theory which limited the value of the aerodynamic damping. The assumption is made to replace σ by $\sin\sigma$ everywhere in the analysis. This assumption is mathematically constant with the actuator disk model. Figure 7 shows the results obtained with this assumption incorporated into the analysis. For $|\sigma| \leq 45°$, the modified analysis yields results that are comparable to those obtained from the original formulation. In addition the modified analysis predicts a finite maximum value for δ_N for $\sigma = 90°$. This maximum value for damping is equal to the value computed at $\sigma = 1$ radian using the original formulation. Experimental results of reference 7 show that this value for σ (i.e., $\sigma = 1$ radian) corresponds rather closely to the measured interblade phase angle of the least stable flutter mode.

An additional validation of the modified analysis as a flutter prediction system for supersonic stall bending flutter can be established by showing that, for a given rotor, flutter will be observed whenever the predicted maximum value of δ_N exceeds the normalized structural damping of a rotor assembly. For this demonstration the measured flutter boundary of a scaled model of Fan C of the NASA Quiet Engine Program (ref. 6) is correlated with the predicted boundary. The performance map for the scale model (fig. 8) shows two flutter instability zones. The first zone is torsional flutter that occurs at part speed and lies close to the stall line. Just above this zone lies a zone of bending flutter that appears to extend past 95 percent of design speed. Only the bending flutter mode of this rotor is analyzed in this paper.

Figure 9 shows a plot of the phase shift between the amplitude time history of a rotor blade and the reference blade No. 17 at the 95 percent of design speed flutter point. The data implies the flutter mode is predominatly a 3 nodal diameter forward traveling wave which corresponds to an interblade phase angle of approximately 41°. This value for the interblade phase angle of the flutter mode correlates well with the data of reference 7 and lies within the unstable range predicted by the analysis. Figure 10 shows the calculated maximum normalized aerodynamic damping for this rotor as a function of weight flow and wheel speed. The results presented on this curve were calculated using the blade element data recorded at the five operating condition shown on figure 8. The shaded region on figure 10 represents the unstable flutter region. The boundary of this region was estimated by assuming a log decrement of 0.025 for the mechanical damping of the assembly (ref. 3). Hence all operating conditions which have an aerodynamic damp-

ing level in excess of this value are assumed to be within the flutter region, while those that have an aerodynamic damping level less than 0.025 are stable.

The results on figure 10 clearly show the significant influence of wheel speed and aerodynamic loading on the aerodynamic damping. The calculated aerodynamic damping at 60 and 70 percent wheel speed lie significantly below the instability boundary. No bending flutter was observed at these operating conditions. At 90 percent of design speed bending flutter was observed near the stall region. The calculated aerodynamic damping for the near stall operating point is seen to lie just inside the unstable region. Bending flutter was also observed at 95 percent of design speed near the stall boundary. The calculated aerodynamic damping for this operating point lies well within the unstable region of figure 10. At the intermediate operating point on the 95 percent speed line the calculated aerodynamic damping falls below the instability boundary. Therefore the predicted flutter boundary at this wheel speed lies between the measured flutter boundary and the intermediate operating point. Transcribing the stability boundary of figure 10 onto the Fan C performance map yields a theoretical flutter boundary, which is shown as a dashed line on figure 11. The measured operating conditions at which bending flutter occurred are shown on this figure as solid symbols. The overall agreement between theory and measurement is very good, with the analysis slightly over predicting the extent of the flutter boundary at 95 percent of wheel speed. Below 90 percent of wheel speed the analysis predicts the flutter boundary will bend back into the stall region. This result is confirmed by the experimental measurements.

The results presented in this section clearly show that the current analysis can be used to predict the onset of supersonic bending flutter in unshrouded fans. The input variables to the analysis can all be derived from fan structural and aerodynamic design variables. The governing equations are simple algebraic equations, and hence are easily programmed. These features provide the designer with a simple and reliable model for analyzing the susceptibility of a fan design to supersonic stall bending flutter. In addition it provides him with a tool that can also be used to evaluate proposed fixes to an existing flutter problem.

The engineering approximation introduced to extended the range of validity of actuator disk theory appears reasonable. To develop a correct first principles extension of actuator disk theory to finite interblade phase angle for the flow conditions as they exist at the tip of a rotor at the onset of supersonic stall flutter would require a viscous transonic cascade analysis for finite interblade phase angle. No such analysis appears to be forth coming in the near future. Any extension which is derived from inviscid aerodynamic theory would be an approximation, the result perhaps being no more accurate then the simple extension developed in this analysis.

CONCLUDING REMARKS

In the present investigation an analytical model was developed to predict the onset of supersonic stall bending flutter in high-speed rotors. The stability boundary predicted by the analysis was shown to be in good agreement with the measured boundary of a high speed fan. The analysis also predicted that the flutter mode would be a forward traveling wave, be sensitive to wheel speed and aerodynamic loading. This was confirmed by the experimental measurements. In addition the analysis showed that reduced frequency and dynamic head also play a significant role in establishing the supersonic stall bending flutter boundary of an unshrouded fan.

This analysis provides the designer with a simple and efficient prediction tool which he can use to analyze the susceptibility of a fan design to supersonic stall bending flutter.

APPENDIX A

SYMBOLS

b	airfoil semichord
c	average blade chord and damping coefficient
d	circumferential distance around wheel
F_i	aerodynamic force
h_1	axial displacement of an airfoil
h_2	tangential displacement of an airfoil
i	$\sqrt{-1}$
K	constant
k	reduced frequency based on circumferential distance, $\omega d/q_\infty$
k_b	reduced frequency based on semichord, $\omega b/q_\infty$
k_2	wave number of disturbance along cascade plane
M	Mach number
M_b	mass of a rotor blade per unit length
N	number of blades in rotor
n	integer
n_i	unit vector
P	total pressure
p	static pressure
q	magnitude of velocity field
R	radial distance
s	entropy
T	temperature
t	time
U_i	velocity components
U_n	relative velocity component normal to disk
U^R	rotational velocity

W_{Aero}	aerodynamic work per cycle of motion
W_D	energy dissipated per cycle of motion by mechanical damping
w	mass flow rate
x_i	spacial coordinates
α	incidence angle
β	flow angle
γ	ratio of specific heats; axial wave number
δ	log decrement; deviation angle, eq. (13), eq (15)
δ_{m_1}	metal angle at leading edge
δ_{m_2}	metal angle at trailing edge
α'	stagger angle
μ	solidity
ξ	amplitude of blade motion
ρ	density
σ	interblade phase angle
τ	cascade pitch or average thickness of a rotor blade
ϕ	velocity potential
χ	total-pressure-loss coefficient
ω	frequency of oscillation

SUBSCRIPTS

$-\infty$	upstream variable
$+\infty$	downstream variable

SUPERSCRIPTS

$(\bar{})$	steady-state variable
$(\tilde{})$	time-dependent variable
*	complex conjugate
Rel	relative component

REFERENCES

1. Kurosaka, M., "On the Unsteady Supersonic Cascade with a Subsonic Leading Edge - An Exact First Order Theory: Parts 1 and 2," Journal of Engineering for Power, Vol. 96, No. 1, Jan. 1974, pp. 13-31.

2. Verdon, J. M. and McCune, J. E., "Unsteady Supersonic Cascade in Subsonic Axial Flow," American Institute of Aeronautics and Astronautics Journal, Vol. 13, No. 2, Feb. 1975, pp. 193-201.

3. Snyder, L. E. and Commerford, G. L., "Supersonic Unstalled Flutter in Fan Rotors; Analytical and Experimental Results," Journal of Engineering for Power, Vol. 96, No. 4, Oct. 1974, pp. 379-386.

4. Goldstein, M. E., Braun, W., and Adamczyk, J. J., "Unsteady Flow in a Supersonic Cascade with Strong In-Passage Shocks," Journal of Fluid Mechanics, Vol. 83, Pt. 3, Dec. 5, 1977, pp. 569-604.

5. Ruggeri, R. S. and Benser, W. A., "Performance of a Highly Loaded Two-Stage Axial-Flow Fan," NASA TM X-3076, 1974.

6. Giffin, R. G., Parker, D. E., and Dunbar, L. W., "Experimental Quiet Engine Program Aerodynamic Performance of Fan C. General Electric Co., Cincinnati, OH, Aug. 1972. (NASA CR-120981)

7. Loiseau, H., and Maquennehan, B., "Aeroelastic Instabilities in Compressors and Tests in a Rectilinear Blade Cascade Wind Tunnel," Revue Francaise de Mecanique, Special Issue, 1976, pp. 157-167.

8. Whitehead, D. S., Bending Flutter of Unstalled Cascade Blades at Finite Deflection," R&M-3386, British Aeronautical Research Council, 1965.

9. Whitehead, D. S., "The Vibration of Cascade Blades Treated by Actuator Disc Methods," Institution of Mechanical Engineers (London), Proceedings, Vol. 173, No. 20, 1959, pp. 555-563.

10. Adamczyk, J. J., "Analysis of Supersonic Stall Bending Flutter in Axial-Flow Compressor by Acutator Disk Theory," NASA TP-1345, 1978.

11. Johnsen, I. A. and Bullock, R. O., eds., "Aerodynamic Design of Axial-Flow Compressors," NASA SP-36, 1965.

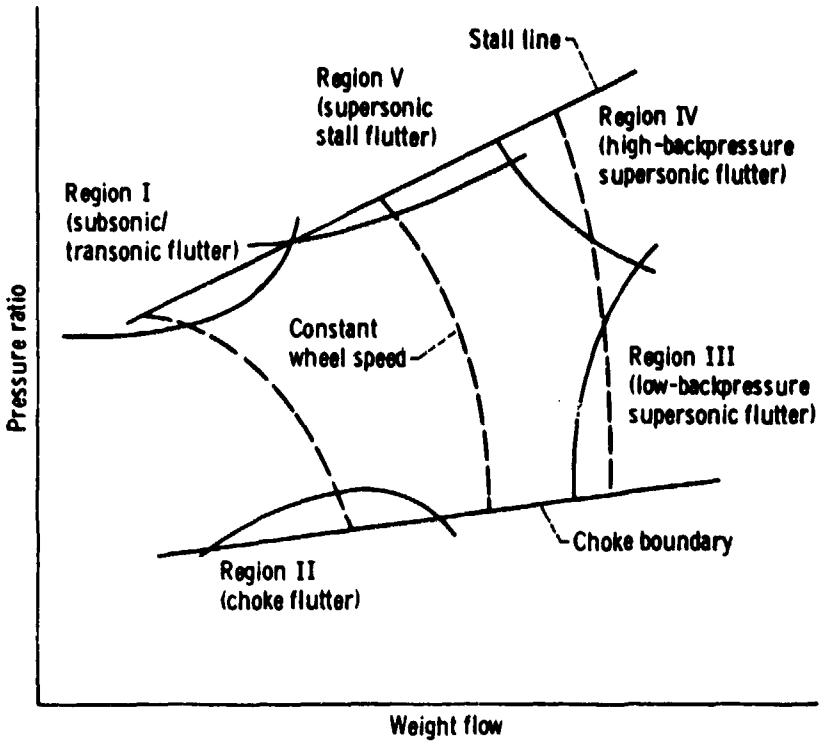

Figure 1. - Compressor performance and stability map.

Curve	Static pressure	
	kN/m^2	(psia)
1	82	(12)
2	89	(13)
3	96	(14)
4	103	(15)
5	110	(16)
6	117	(17)
7	124	(18)
8	131	(19)
9	137	(20)
10	144	(21)

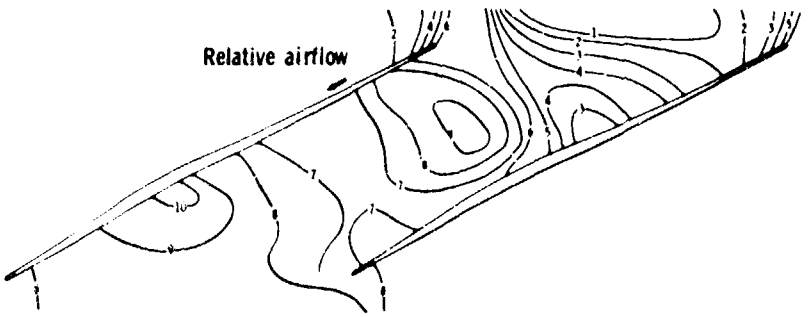

Figure 2. - Typical tip rotor static-pressure distribution near supersonic stall flutter boundary.

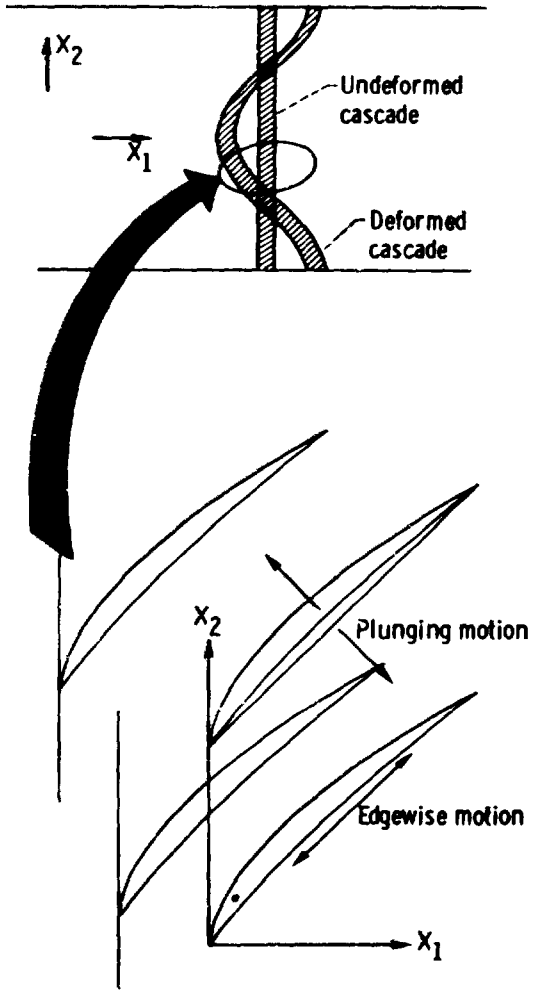

Figure 3. - Cascade plane deformation.

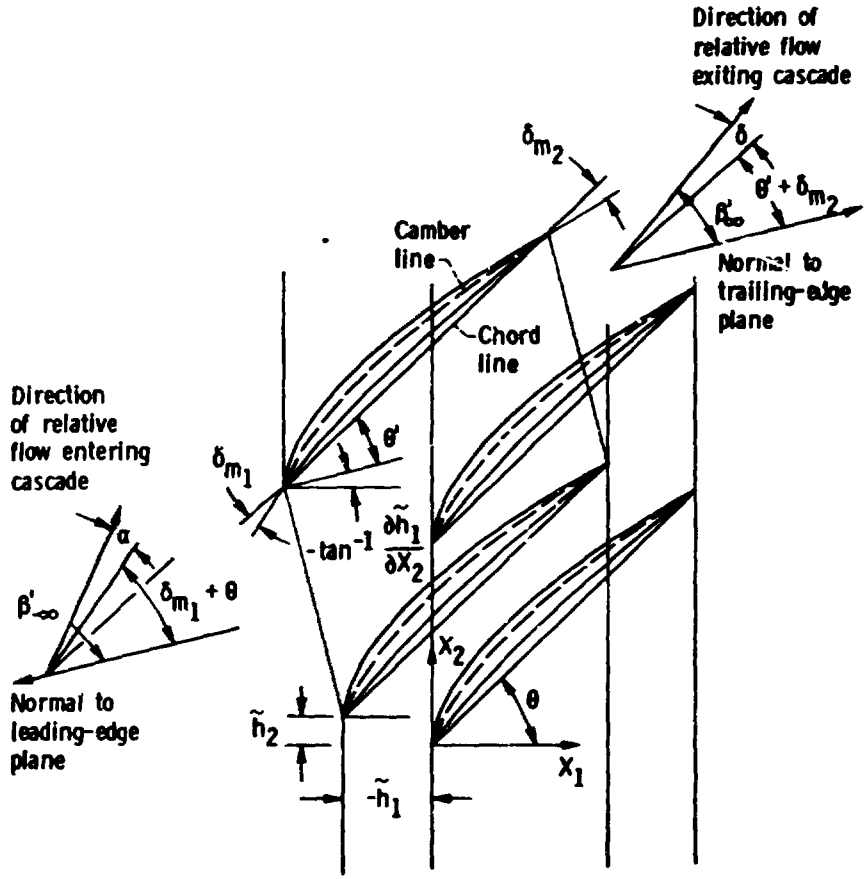

Figure 4. - Geometry of deformed cascade.

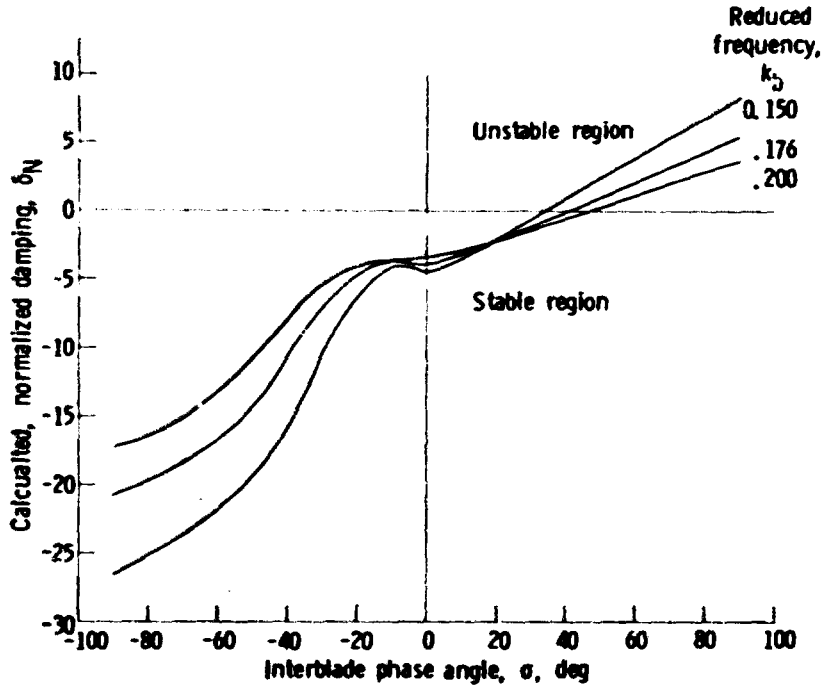

Figure 5. - Calculated, normalized damping as a function of interblade phase angle and reduced frequency for NASA two-stage fan.

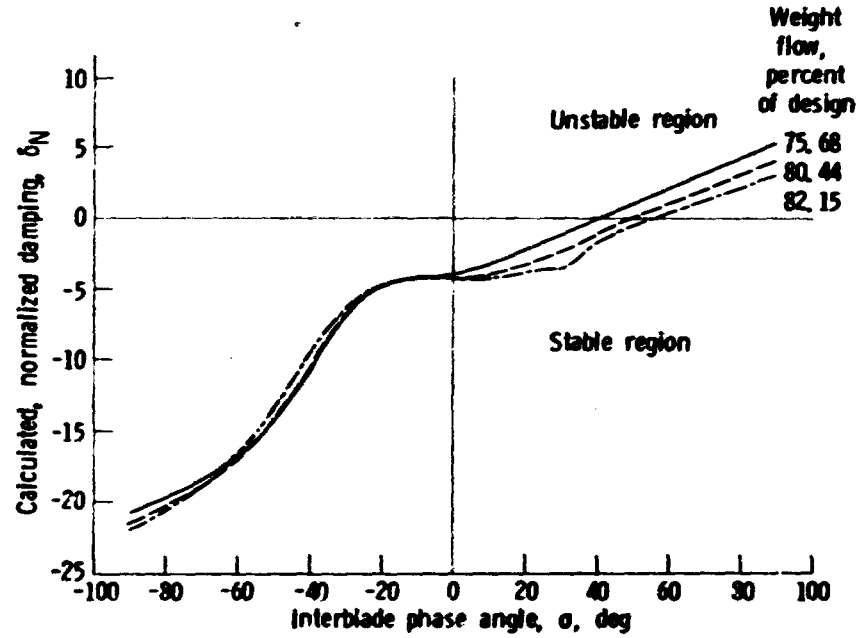

Figure 6. - Calculated, normalized damping as a function of interblade phase angle and weight flow for NASA two-stage fan at 85 percent of design wheel speed.

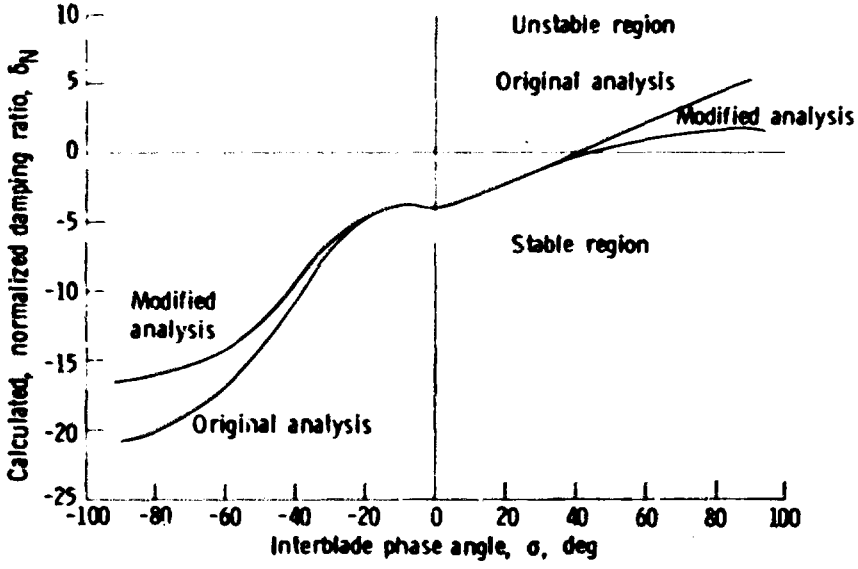

Figure 7. - Original and modified analyses for NASA two-stage fan at 85 percent of design wheel speed and 75.68 percent of design weight flow.

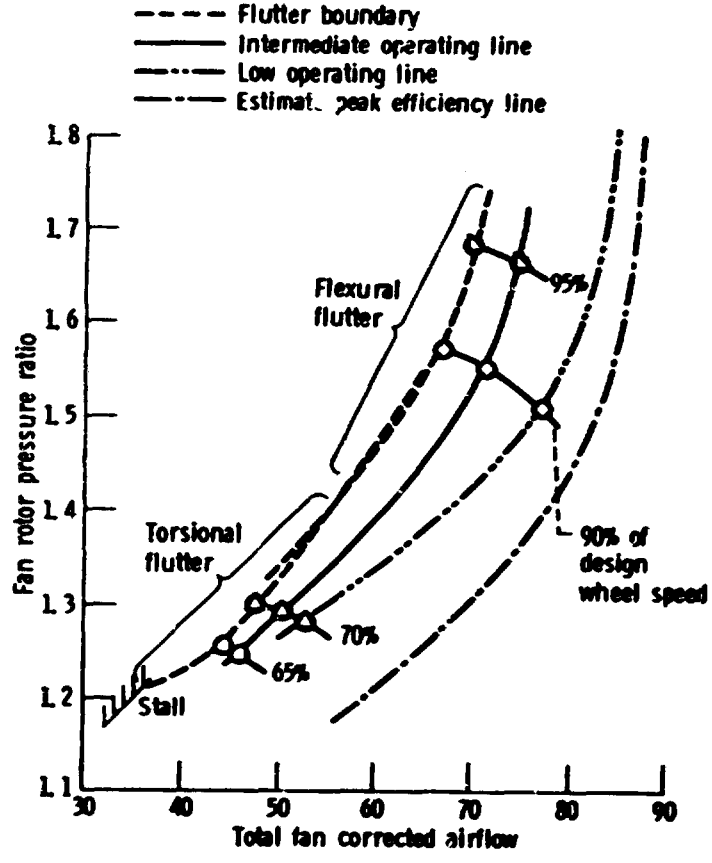

Figure 8. - NASA rotating rig, fan C model.

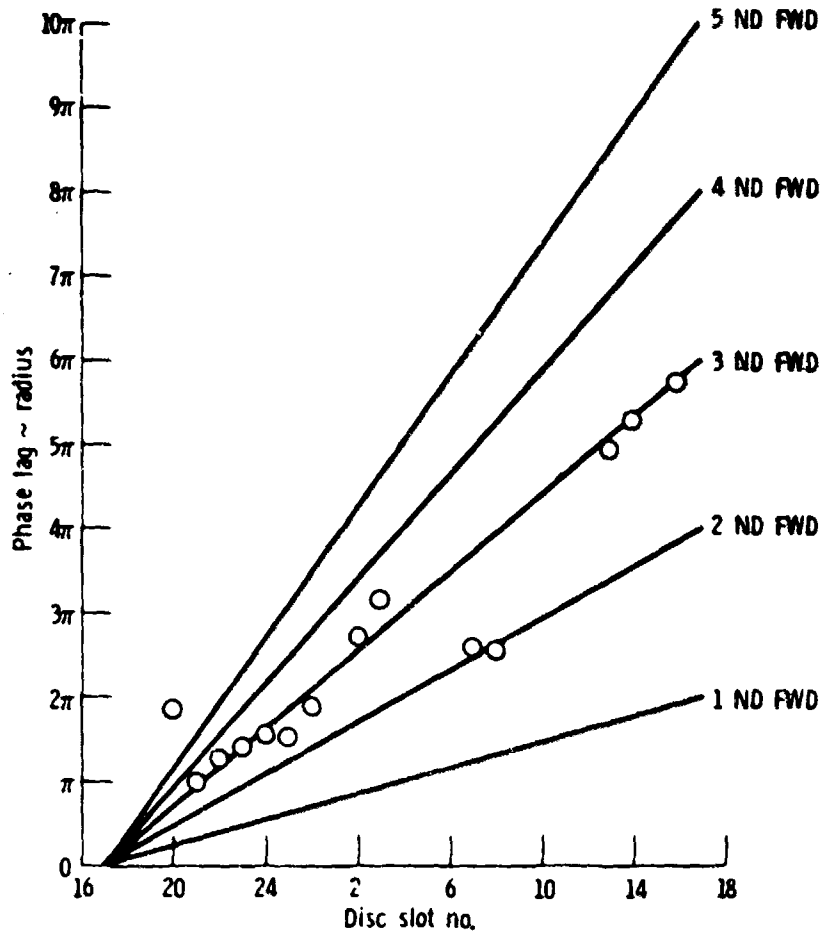

Figure 9. - Rotating rig blade phase data 95% speed, flexural flutter.

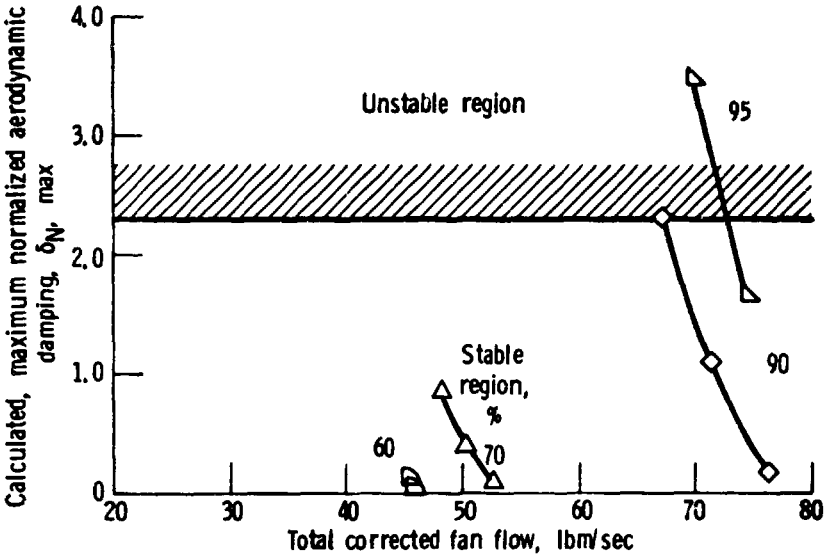

Figure 10. - Maximum normalized damping as a function of weight flow and wheel speed for fan C model.

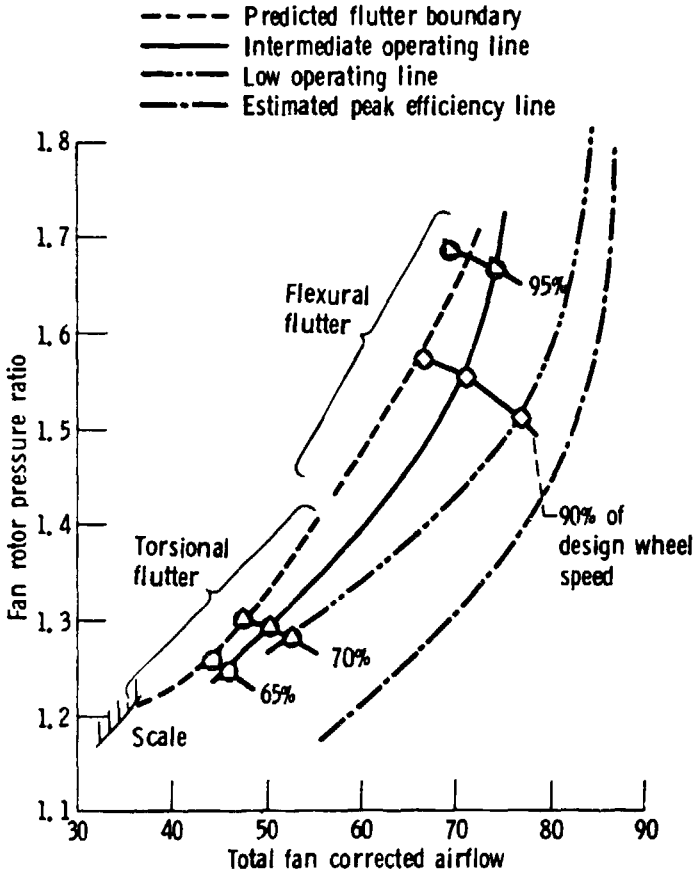

Figure 11. - NASA rotating rig, fan C model.